



Intermediate-induced repolymerization for constructing self-assembly architecture: Red crystalline carbon nitride nanosheets for notable hydrogen evolution

Sufeng An^a, Yongkang Guo^a, Xiaoyu He^a, Pan Gao^b, Guangjin Hou^b, Jungang Hou^{a,*}, Chunshan Song^c, Xinwen Guo^{a,*}

^a State Key Laboratory of Fine Chemicals, PSU-DUT Joint Center for Energy Research, School of Chemical Engineering, Dalian University of Technology, Dalian 116024, China

^b Dalian Institute of Chemical Physics, Chinese Academy of Sciences, Dalian 116023, China

^c Department of Chemistry, Faculty of Science, The Chinese University of Hong Kong, Shatin, NT, Hong Kong, China

ARTICLE INFO

Keywords:

Crystalline carbon nitride
Self-assembly structure
Intermediate-induced strategy
Synergistic optimization
Solar hydrogen production

ABSTRACT

Few-layered polymeric carbon nitride (PCN) nanosheets with large specific surface area and effective charge/electron transport pathway have emerged as promising photocatalysts. However, PCN nanosheets normally exhibit enlarged bandgap, structural defects, and easy agglomeration. Herein, we report an intermediate-induced strategy for synthesizing red PCN nanosheets with a crystalline free self-assembly (CFSA) architecture, exhibiting a three-dimensional (3D) structure, minimum structural defects, small curved nanosheet subunits, and abundant reactive sites. The careful tuning of the condensation degree and repolymerization ability of intermediates affords CFSA PCN with an optimal 3D structure and optical properties, enabling the synergistic optimization of light absorption, charge mobility, and surface reactions during photocatalysis. The catalyst shows a superior H₂ evolution rate of 14665 $\mu\text{mol g}^{-1} \text{h}^{-1}$ (Pt 1.1 wt%), outperforming those of pristine bulk and nanosheet-structured PCN. This work provides a facile intermediate-induced strategy for guiding the design and synthesis of novel PCN-based photocatalysts.

1. Introduction

Photocatalytic water splitting for H₂ production is a promising approach for converting solar energy into clean chemical energy [1,2]. Unfortunately, the efficiency of solar-to-hydrogen energy conversion is still very low after decades of research [3,4], therefore, considerable efforts are being devoted to the exploration of novel photocatalysts the critical processes in photocatalysis, i.e., optical absorption, exciton dissociation, and surface reactions. In this context, polymeric carbon nitride (PCN) has garnered considerable interest for solar energy conversion owing to its chemical and thermal stabilities, metal-free nature, and visible-light response [5–8]. However, pristine PCNs synthesized using the traditional thermal polycondensation of nitrogen-containing precursors typically inherits their drawbacks such as high recombination of photoinduced charges, restricted visible-light absorption, and low crystallinity and specific surface area, thus hindering the optimization of the aforementioned critical processes in photocatalysis [9–11].

Thus, pristine PCNs show low photocatalytic activity far below theoretical expectations.

Unique nanostructured photocatalysts typically exhibit distinct physical, optical, and electronic properties [12–14]. In particular, PCN—as a conjugated polymer semiconductor—can show various nanostructures such as mesoporous structures, nanorods, hollow spheres, and nanosheets, which can be modified feasibly by controlling the polycondensation process [15–18]. Among these nanostructures, few-layered PCN nanosheets with large specific surface area and effective charge/electron transport pathway (in other words, decreased perpendicular migration distance for charge carriers from the bulk to the surface and accelerated electron transport along the in-plane direction, respectively) exhibit considerable advantages for promoting photocatalytic efficiency [12]. To synthesize PCN nanosheets, various strategies including template methods, thermal oxidation etching, and solvent-assisted ultrasonic exfoliation have been developed [19–21]. Unfortunately, because of strong chemical etching or excess physical

* Corresponding authors.

E-mail addresses: jhou@dlut.edu.cn (J. Hou), guoxw@dlut.edu.cn (X. Guo).

<https://doi.org/10.1016/j.apcatb.2022.121323>

Received 16 December 2021; Received in revised form 16 February 2022; Accepted 13 March 2022

Available online 17 March 2022

0926-3373/© 2022 Elsevier B.V. All rights reserved.

exfoliation, the surface of such PCN nanosheets inevitably presents structural defects. These structural defects serve as charge trap sites during photocatalysis, limiting the photocatalytic activity of the PCN nanosheets. To reduce the number of structural defects during PCN synthesis and improve the PCN crystallinity, the use of eutectic salts (LiCl, NaCl, and KCl) during thermal condensation is the most popular strategy [22–24]. However, this strategy generally affords bulk crystalline PCN, which requires further ultrasonic exfoliation to produce crystalline PCN nanosheets exhibiting a graphene-like morphology with a large aspect ratio and a long charge transport pathway along the in-plane direction [25]. Moreover, the PCN nanosheets obtained using the aforementioned methods show an enlarged bandgap because of the quantum confinement effect [20,26]. Consequently, PCN nanosheets typically exhibit poor wide-spectrum visible-light absorption capability and limited visible-light photocatalytic performance. Overall, the existing approaches for synthesizing PCN nanosheets cannot simultaneously improve the optical absorption, exciton dissociation, and surface reactions, essential for enhancing the photocatalytic performance. Therefore, the development of an effective strategy for fabricating novel optimized PCN nanosheets is highly desirable.

Herein, we report an intermediate-induced strategy to synthesize crystalline free self-assembly (CFSA) PCN (Ux-670) consisting of small curved nanosheets connected continuously, which were expected to exhibit optimized structural and optical properties. The morphology and properties of the CFSA structure could be tuned using intermediate species (Ux, $x = 300\text{--}550$, where x represents the precondensation temperature of urea) obtained by preheating urea at different temperatures. Based on thorough scanning electron microscopy (SEM), transmission electron microscopy (TEM), thermogravimetric analysis (TGA), Fourier transform infrared (FT-IR), ^{13}C cross polarization/magic angle spinning (CP-MAS) nuclear magnetic resonance (NMR), and in situ X-ray diffraction (XRD) analyses, the condensation degree and repolymerization ability of the intermediates were found to be key factors in the construction of an advanced CFSA structure. The U350 intermediate with a moderate condensation degree and repolymerization ability promoted the formation of a continuous 3D CFSA structure of PCN (denoted as U350–670) during the second polymerization stage. In the photocatalytic H_2 production from water, U350–670 exhibited significantly improved H_2 evolution rate than pristine bulk and nanosheet-structured PCN. This intermediate-induced strategy employing the careful tuning of the condensation degree and repolymerization ability of intermediates offers a new platform for constructing crystalline 3D PCN nanosheets, thus overcoming the inherent disadvantages of conventional PCN nanosheets.

2. Experimental section

2.1. Materials

Triethanolamine (TEOA), urea, and chloroplatinic acid ($\text{H}_2\text{PtCl}_6 \cdot 6\text{H}_2\text{O}$) were purchased from Aladdin (Shanghai, China). All chemicals were used without further purification.

2.2. Catalyst characterization

FT-IR spectra of the Ux-670 samples were recorded on an FT-IR spectrometer (Thermo Fisher Scientific, Nicolet iS50) equipped with a DTGS detector. Powder XRD patterns were recorded on an X-ray diffractometer (Smart Lab 9, Rigaku Corporation) with a nickel-filtered $\text{Cu K}\alpha$ X-ray source at a scanning rate of 0.02° between 5° and 80° , a tube voltage of 45 kV, and a current of 200 mA, respectively. X-ray photoelectron spectroscopic (XPS) measurements were carried out on a spectrometer (ESCA Lab250, Thermo Scientific Fisher) with a monochromatic $\text{Al K}\alpha$ X-ray source; the binding energy was estimated using the $\text{C } 1\text{ s}$ peak at 284.6 eV. The SEM images of Ux-670 were obtained using a scanning electron microscope (SU8220, Hitachi, Japan). The

TEM images were obtained on a transmission electron microscope (HT7700 EXALENS, Hitachi, Japan) with an acceleration voltage of 100 kV. The atomic force microscopic (AFM) images of PCN were recorded (NanoWizard ULTRA Speed and inVia Raman, Bruker JPK). The thickness of the nanosheets was analyzed using JPK SPM Data Processing software. The ultraviolet–visible (UV–vis) spectra of PCN were collected on a JASCO V-550 spectrometer. Photoluminescent (PL) spectroscopy was performed on a JASCO FP-6200 spectrofluorometer at an excitation wavelength of 310 nm. Electron paramagnetic resonance (EPR) spectroscopy was performed at room temperature using an E500 spectrometer (Bruker, Germany).

2.3. Synthesis of U550

Urea (20 g) was pyrolyzed at 550°C for 3 h in a muffle furnace at a ramping rate of 5°C min^{-1} . The synthesized slight yellow powder was denoted as U550.

2.4. Synthesis of Ux-670 ($x = 300\text{--}550$)

First, urea (20 g) was pyrolyzed at different temperature (300°C , 350°C , 400°C , 450°C , 500°C , and 550°C) for 3 h in a muffle furnace at a ramping rate of 5°C min^{-1} . The prepolymerized powders were used as concentrated intermediates of PCN (denoted as Ux, $x = 300\text{--}550$). Then, a certain amount of Ux intermediates were further calcined at 670°C in a tube furnace at a ramping rate of 5°C min^{-1} in an inert atmosphere. Before calcination, the tube furnace was purged by vacuuming and back filling with N_2 for two times. Powders of different colors were afforded after holding them at 670°C for 2 h and cooling, denoted as Ux-670 ($x = 300\text{--}550$).

2.5. Photocatalytic H_2 generation

Photocatalytic H_2 production using the Ux-670 samples was evaluated in a Pyrex top-irradiation reaction vessel (150 mL) at 25°C and cooled using a circulating cooling system under visible-light irradiation. In a typical process, 10 mg catalyst and Pt cocatalyst (1.1 wt%) were added to 30 mL deionized water. The mixture was ultrasonicated for 10 min and stirred for 1 h. After adding 10 vol% TEOA in the mixture, the suspension was purged with Ar for 15 min to remove air and sealed at ordinary pressure. The reaction solution was irradiated using a 300 W Xe arc lamp (PLS-SXE 300CUV, Beijing Perfect Light Technology Co. Ltd., China) with a cutoff filter of 420 nm. The H_2 production was detected using gas chromatography with a TCD detector.

2.6. Photoelectrochemical measurement

The transient photocurrent was measured on an electrochemical workstation (CHI660D, Shanghai, China). A platinum wire and Ag/AgCl electrodes were used as counter and reference electrodes, respectively. The working electrode was fluorine-doped tin oxide glass ($1 \times 1\text{ cm}$) coated with the catalysts. The slurry comprised 5 mg of the Ux-670 sample dispersed in 950 μL ethanol and 100 μL Nafion solution. The electrolyte solution was 0.2 M Na_2SO_4 , and a 300 W Xe lamp ($\lambda > 420\text{ nm}$) was used as the light source. Electrochemical impedance spectra (EIS) were recorded in a frequency range of 0.01–105 Hz with an open-circuit voltage.

3. Results and Discussion

3.1. Synthesis and characterization of PCN samples

The intermediate-induced strategy for synthesizing free self-assembly (FSA) PCN samples is based on our previously reported method (Fig. 1a) [27]. First, precondensed intermediates (labeled as Ux, $x = 300\text{--}550$) with different condensation degrees were obtained by

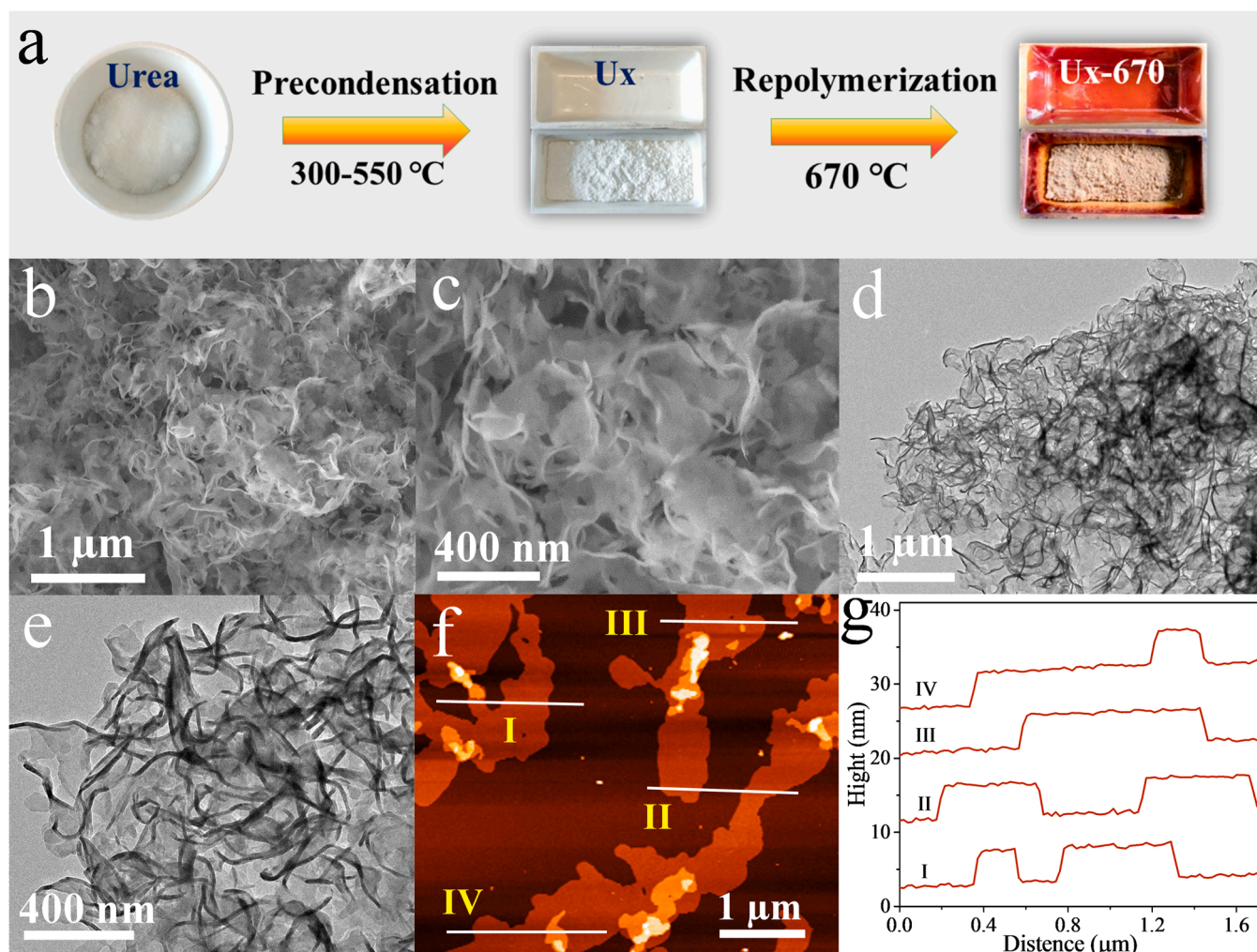


Fig. 1. (a) Illustration of the synthesis procedure of Ux-670 samples, (b, c) SEM, (d, e) TEM, (f) AFM images and (g) the corresponding thickness analysis taken around the white line in (f) of U350–670.

preheating urea at different temperatures (300 °C, 350 °C, 400 °C, 450 °C, 500 °C, and 550 °C) for 3 h in an air atmosphere, aiming to overcome the easy sublimation and decomposition of urea under high-temperature pyrolysis. Subsequently, the Ux intermediates were further heated to 670 °C for 2 h in an inert atmosphere. The precondensation and inert atmosphere protection of the Ux intermediates afforded some PCN samples (denoted as Ux-670, $x = 300\text{--}550$) via high-temperature pyrolysis. As shown in Fig. 1b and S1, all the Ux-670 samples comprised highly fluffy and soft agglomerates. Fig. 1c–1e, S2, and S3 display the high-magnification SEM and TEM images of these agglomerates, whose basic subunits consisted of small nanosheets with a lateral scale, smooth surface, and curved edges. These small nanosheet subunits connected freely, forming a continuous FSA framework. In particular, the FSA structure of the U350–670 and U400–670 samples showed a 3D architecture (Fig. 1d, 1e, S2, and S3b), which can prevent the aggregation of the nanosheets, thereby providing abundant active sites. Furthermore, the curved nanosheets and abundant wrinkles in the FSA structure indicated the partial distortion of heptazine-based PCN, potentially facilitating the activation of the $n \rightarrow \pi^*$ electronic transition for enhanced visible-light absorption above 500 nm [28]. These unique characteristics of the 3D FSA structure of the U350–670 and U400–670 samples enabled considerable advantages over other PCN nanosheets with a large aspect ratio [20,25]. Conversely, the U300–670, U450–670, U500–670, and U550–670 samples exhibited a hybrid structure comprising the partial 3D FSA framework and further fragmented

nanosheets (Figs. S1 and S3), indicating that the morphology of the FSA structure highly depended on the type of intermediate species (U300–U550). Compared with the pristine PCN nanosheets (U550), the Ux-670 samples exhibited higher specific surface area which increases first and then decreases with the increase of prepolymerized temperature (Table S1), consistent with the morphological change tendency of Ux-670 samples.

The morphology and thickness of the nanosheet subunits in the FSA structure were studied using AFM (Fig. 1f and 1g). The nanosheets showed a uniform thickness of ~ 4.2 nm, which is thicker than the thickness of PCN nanosheets (~ 2 nm) synthesized using the thermal oxidation method [20]. These nanosheets with an increased thickness in the FSA structure afforded a 3D framework owing to the strong strain force. Moreover, the nanosheets showed a smooth surface and irregular shapes similar to spliced structures formed by small nanosheets, as observed in the SEM and TEM results. The smooth nanosheet surface indicated the enhanced planar structure and crystallinity of PCN, which can also be confirmed using electron diffraction and high-resolution TEM analyses. The electron diffraction patterns of U350–670 (Fig. 2a) revealed distinct electron diffraction rings in regions I and II, demonstrating the crystalline nature of the FSA structure of PCN. Two lattice fringes were detected in Fig. 2b–2d and S4, further indicating that U350–670 exhibited a CFSA structure. The lattice fringe with a d-spacing of 0.57 nm (Fig. 2c and S4c) can be assigned to the repeating packing distance of the in-plane heptazine units (100) [22,24]. Such a

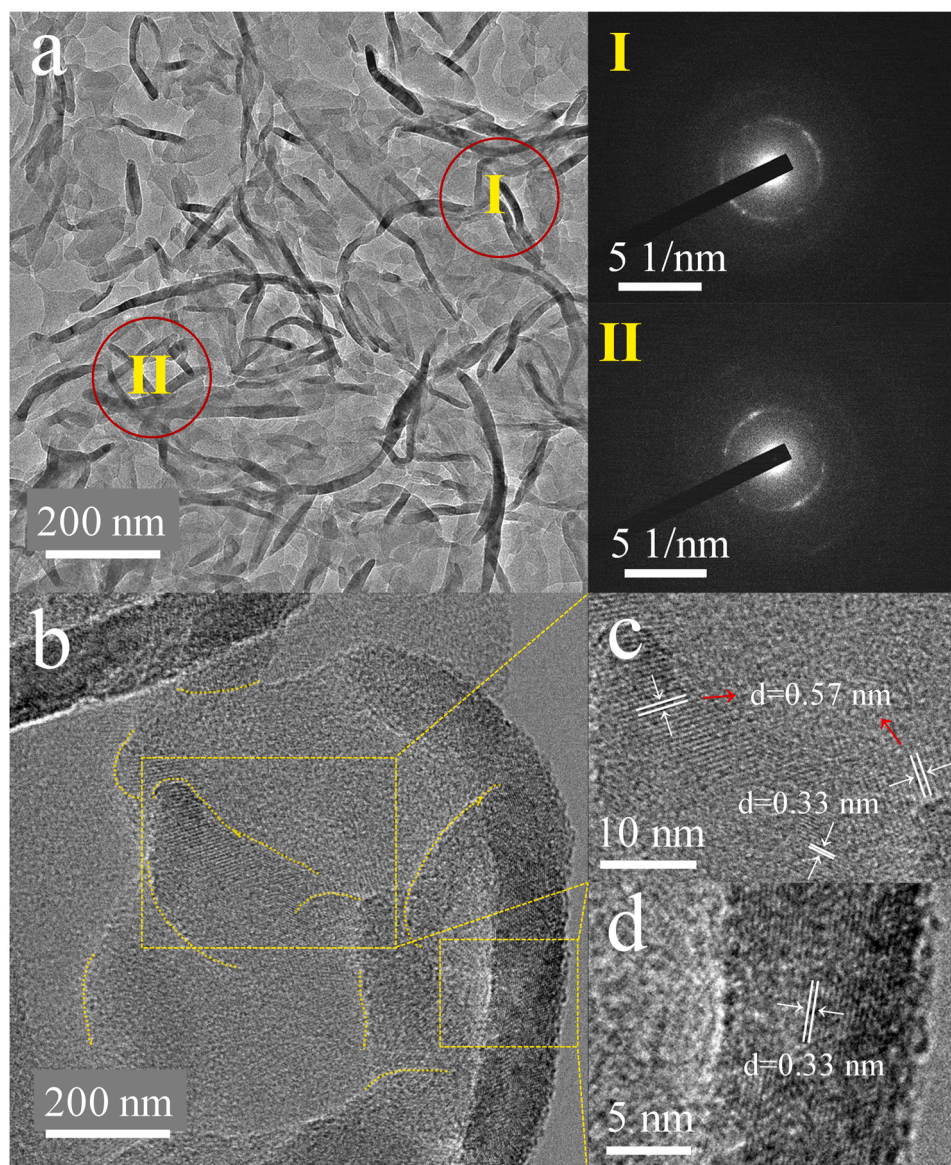


Fig. 2. (a) TEM images and the corresponding electron diffraction patterns of U350-670, (b-d) HRTEM images of U350-670.

decrease in the d-spacing indicated the presence of a well-compact heptazine-based skeleton in U350-670 [28]. Furthermore, the lattice fringe with a d-spacing of 0.33 nm (Fig. 2d and S4b) was attributed to the interlayer stacking distance. Interestingly, the two lattice fringes were anisotropically distributed in the CFSA structure of U350-670, as supported by the electron diffraction rings in Fig. 2a, corresponding to its spliced FSA and distorted structure. The continuous 3D CFSA structure of U350-670 comprising small crystalline curved nanosheets provided abundant active sites and decreased both the bulk and in-plane diffusion lengths for charge carrier transport, thereby improving the charge transfer in the nanosheets [29]. These results demonstrate that a novel PCN with a 3D CFSA structure and enhanced properties was successfully synthesized using the proposed intermediate-induced strategy.

3.2. Mechanism of the intermediate-induced strategy

Next, to gain a deep understanding of the intermediate-induced strategy (Fig. 3a), the condensation degree of the intermediates and the condensation of the nitrogen-containing precursor were investigated using a combination of in situ XRD, TGA, and FT-IR analyses. Based on

the TGA (Fig. 3b) and SEM (Fig. S5) results, the Ux intermediates exhibited notably different condensation degrees, which increased in the following order: urea < U300 < U350, U400 < U450, U500, and U550, this was evidenced by their distinctly diverse weightlessness temperatures and morphologies. Intermediates with an excessively high polymerization degree cannot undergo further condensation reactions at high temperatures, as in the case of the U450, U500, and U550 intermediates, which showed similar weightlessness temperatures and integral polymer morphologies [9]. Conversely, intermediates showing a considerably low condensation degree—such as U300, would suffer from excessive weightlessness at high temperatures. To construct a continuous 3D CFSA structure comprising small curved nanosheet subunits, the Ux intermediates should possess moderate condensation degree, namely, the generation of subunits, and repolymerization ability, namely, the ability of the subunits to connect with each other, during the second polymerization stage (Fig. 3a: Route 2). In Fig. 3c, two distinct peaks at 164.5 and 156.5 ppm ascribed to the $C_{(e)}$ atoms (N_2 -CN or terminal $CN_2(NH_x)$) and $C_{(i)}$ atoms (CN_3), respectively, were observed of U350, U400, U450, and U550, confirming the presence of heptazine-based units in these Ux intermediates. Based on the TGA, ^{13}C CP-MAS NMR, XRD, and FT-IR results, the U350 and U400

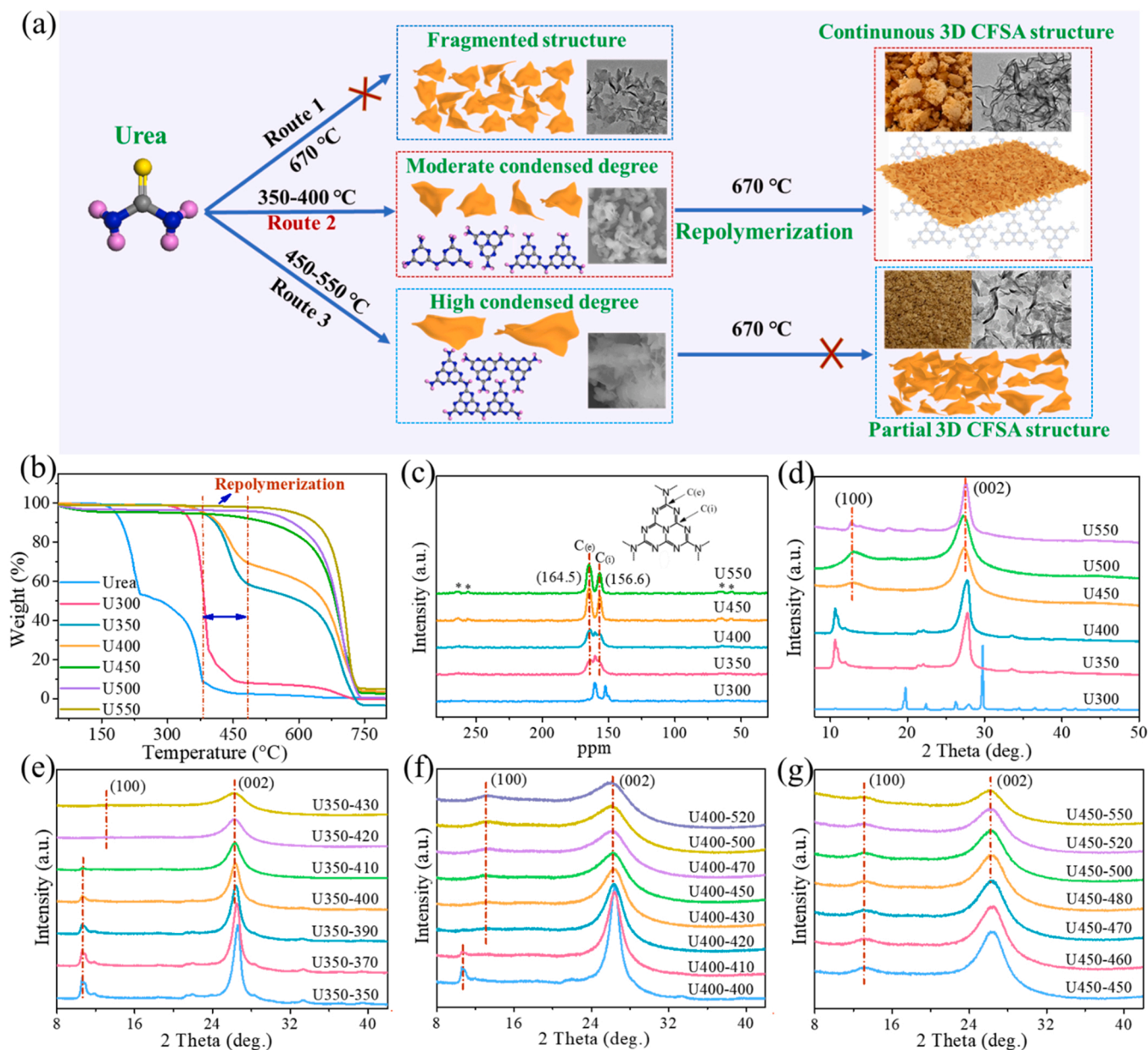


Fig. 3. (a) Illustration of the intermediate-induced strategy, (b) TG curve of U_x intermediates in N₂ atmosphere, (c) ¹³C CP-MAS NMR and (d) XRD patterns of U_x intermediates, in-situ XRD patterns of (e) U350, (f) U400 and (g) U450 intermediates.

intermediates showed moderate thermal stability (~ 380 °C, Fig. 3b) and contained oligomeric intermediate species such as melam and melem (Fig. 3c, 3d, and S6) [9,30,31]. Moreover, the two intermediates exhibited certain repolymerization ability during the second pyrolysis stage at high temperatures, evidenced by their moderate weightlessness at 380–480 °C (Fig. 3b). This result was further confirmed by the in situ XRD patterns (Fig. 3e), in which the diffraction peaks of U350 changed considerably as the temperature increases from 350 °C to 420 °C, indicating that the U350 intermediate could induce further repolymerization reactions to form a continuous 3D CFSA structure (Fig. 3a: Route 2). Similarly, the U400 intermediate could induce a repolymerization reaction during the second pyrolysis stage; however, this distinctly occurred at a narrow temperature range of 400–420 °C (Fig. 3f). In contrast, two typical diffraction peaks were detected in the XRD patterns of U450, U500, and U550 (Fig. 3d), corresponding to the (100) and (002) planes of the heptazine-based structure. Furthermore, the in situ XRD pattern of U450 did not exhibit any apparent change when the

temperature was increased from 450 °C to 550 °C (Fig. 3g). These results demonstrate that a primary assembly interlayer and an in-plane heptazine-based PCN structure were formed in the intermediates (U450, U500, and U550) during the preheating stage, endowing them with high thermal stability (~ 600 °C) and similar ¹³C CP-MAS NMR spectra (Fig. 3c). Owing to the high polymerization degree of U450, U500, and U550, they cannot undergo further repolymerization reactions during the second pyrolysis stage (Fig. 3a: Route 3). Instead, the partial decomposition of the heptazine-based structure may occur at high temperatures, thereby affording the fragmentized nanosheet structure (Fig. S1) of U450–670, U500–670, and U550–670. Note that U300 and urea with a low condensation degree, which do not contain primary polymeric subunits such as melam and melem according to their ¹³C CP-MAS NMR spectra (Fig. 3c) and in situ XRD patterns (Fig. S7), were also unfavorable for the formation of the continuous 3D CFSA structure (Fig. 3a: Route 1) of PCN, as shown in the SEM (Figs. S1a and S1f) and TEM (Figs. S3a and S3f) images. Based on these results, the U350

intermediate with moderate condensation degree and repolymerization ability was selected as the optimal candidate for PCN synthesis with a novel 3D CFSA structure using the intermediate-induced strategy (Fig. 3a: Route2).

3.3. Structural and optical properties of PCN samples

Next, the CFSA PCN structures were examined using XRD, FT-IR/FTIR, and XPS. Compared with the pristine PCN nanosheets (U550), the XRD patterns of all the Ux-670 samples revealed narrow and strong diffraction peaks (Fig. S8a–c), indicating the high crystallinity of the Ux-670 samples. Moreover, a high-angle shifting of the (002) peak in the patterns of Ux-670 confirmed its compact interlayer stacking distance (Fig. S8b). Interestingly, the XRD patterns of Ux-670 differed from those of other reported crystalline heptazine-based PCN derivatives synthesized using the eutectic salt method, whose XRD patterns showed a (100) peak at 8–9°, attributed to the insertion of K^+ , Na^+ , or Li^+ between the heterocyclic units [32]. Unfortunately, owing to the partially distorted and anisotropically distributed lattices of Ux-670, further information on its crystalline structure could not be obtained from the XRD results. The FT-IR spectra of Ux-670 are presented in Fig. S8d. All the samples showed FT-IR absorption peaks in the fingerprint bands between 1200 and 1640 cm^{-1} , which can be ascribed to a typical heptazine-based skeleton of PCN [33]. In the C1s XPS spectra of Ux-670 (Fig. S9), the primary C1s peak at 288.2 eV corresponded to sp^2 -hybridized carbon ($N-C=N$) in the N-containing aromatic ring. Another small peak with a binding energy of 284.6 eV could be assigned to impurity carbons, such as $C-C/C=C$ species [34]. The N1s spectra can be deconvoluted into

four peaks with binding energies of 398.6, 400.0, 401.1, and 404.3 eV, representing the sp^2 -hybridized $C=N-C$ bonds in the heterocycle ring, sp^3 -hybridized $N-(C)_3$ groups connecting the joint heptazine system, residual $C-NH_x$ species, and charge effects in the aromatic rings, respectively (Fig. S10) [35,36]. These results confirm the presence of heptazine-based units in the CFSA structure in accordance with the XRD and FT-IR results. Moreover, the C1s and N1s peaks of all the Ux-670 samples shifted toward the higher binding-energy region compared with those of the U550 sample (Figs. S9h and S10h), suggesting the presence of a compact heptazine-based skeleton in Ux-670, consistent with its crystalline structure and smaller in-plane d-spacing of 0.57 nm. In addition, based on the XPS results (Table S1), the C/N ratios of the Ux-670 samples ($x = 300, 350, 400$, and 450) were higher than those of the pristine PCN nanosheets and close to 0.75, which was the calculated value for a perfect C_3N_4 polymer [6]. Alternatively, the C/N ratios of U500–670 and U550–670 obviously increased. These results—along with the fragmentized nanosheet structure of the samples (Fig. S1)—indicated the preferential delamination of nitrogen atoms on the U500 and U550 intermediates, in which the polymerization degree was excessively high during the second pyrolysis stage at high temperatures, inducing the partial distortion and decomposition of the heptazine-based structure. These findings further demonstrate that the Ux intermediates with moderate condensation degree and repolymerization ability could induce a relatively complete repolymerization reaction, affording PCN with a continuous 3D CFSA structure during the second pyrolysis stage at 670 °C. This was also evidenced by the presence of reduced $C-NH_x$ species in the XPS spectra of Ux-670 (Fig. S10 and Table S1).

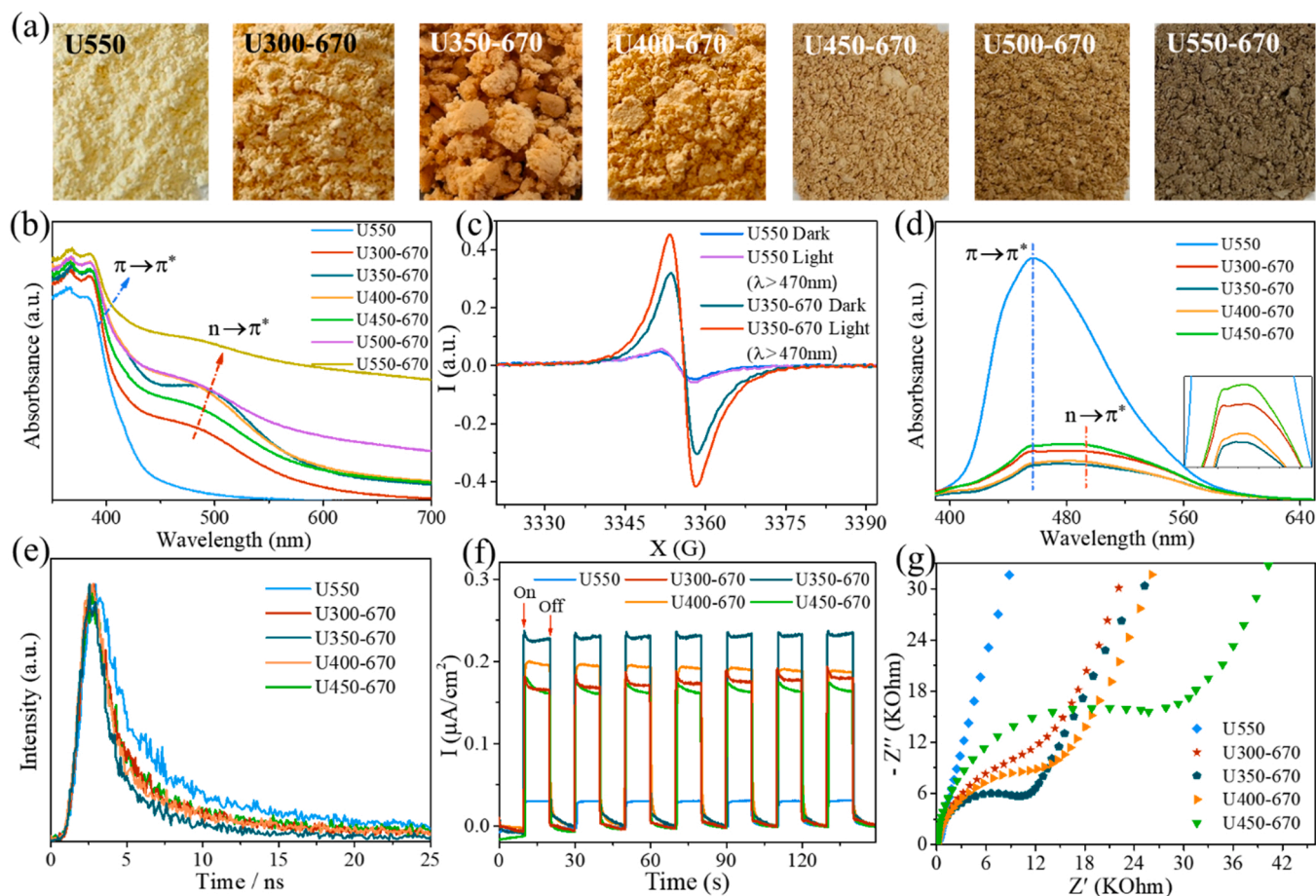


Fig. 4. (a) appearance colors, (b) UV/Vis spectra, (c) EPR spectra, (d) PL spectra and (e) time-resolved transient PL spectra of PCN samples, (f) Photocurrent-potential curves for ITO/U550, ITO/Ux-670 at -1.0 V vs. Ag/AgCl in 0.2 M Na_2SO_4 exposed to visible-light ($\lambda > 420$, 300 W Xe lamp), (g) Nyquist plots of ITO/U550, ITO/Ux-670 are measured in same condition without light irradiation.

The morphological changes in the CFSA structure are expected to considerably modify the optical properties and surface electronic structure of Ux-670 [37,38]. The Ux-670 samples exhibited more differences and deeper colors than the U550 samples (Fig. 4a), indicating their wide-spectrum optical absorption properties. Thus, U350–670 and U400–670 with an advanced 3D CFSA structure were characterized by a brick-red color. Correspondingly, as shown in the UV–vis spectra (Fig. 4b), all the Ux-670 samples exhibited enhanced light absorption in both ultraviolet and visible-light spectral regions compared with the U550 sample. Typical absorption edge detected at ~ 460 nm could be assigned to the intrinsic electronic transition ($\pi \rightarrow \pi^*$) of PCN, shifting to the visible-light region because of the expanded π -conjugated aromatic framework of the continuous CFSA structure. Notably, another absorption peak was detected at ~ 490 nm, expanding the photoresponse of Ux-670 to 600 nm. This new visible-light absorption peak could be ascribed to the $n \rightarrow \pi^*$ electronic transition, which is spatially forbidden in perfectly symmetric and planar heptazine-based PCN [28,34,37]. Therefore, the novel CFSA structure of Ux-670 exhibited a distinct curved nanostructure comprising nanosheet subunits that enables the $n \rightarrow \pi^*$ electronic transition. Particularly in the case of U350–670, an obviously convex absorption peak was observed in the UV–vis spectra, assigned to the $n \rightarrow \pi^*$ electronic transition and attributed to its optimal 3D CFSA structure with maximum structural distortion. Note that the intense visible-light absorption over 500 nm observed in the cases of U500–670 and U550–670 was attributed to their blackish color, originating from the excess elimination of nitrogen atoms under high-temperature pyrolysis. These changes in the UV–vis spectra were consistent with the color variation of Ux-670 (Fig. 4a). The band gap energy of pristine PCN nanosheet (U550) estimated from the Tauc plot was calculated to be 2.75 eV (Fig. S11) which was larger than those of U300–670, U350–670 and U450–670 samples (2.70, 2.45 and 2.61 eV, respectively), indicating the enhanced visible-light absorption of Ux-670 samples consistent with the UV/Vis results. The traditional Mott-Schottky methods were measured to estimate the conduction band (E_{CB}) positions of PCNs, as shown in Fig. S12. It could be observed that the E_{CB} of Ux-670 samples was more negative than that of U550, indicating the enhanced reduction capacity of the conduction electrons in Ux-670 samples. Therefore, the Ux-670 samples were promising as efficient photocatalysts for H_2 evolution due to their both enhanced visible-light absorption and reduction capacity.

Fig. 4c shows the room-temperature EPR spectra of U350–670 and U550. Surprisingly, compared with U550, a drastically enhanced EPR intensity was observed in the spectrum of U350–670, indicating the presence of numerous free charge carriers in the 3D CFSA structure [32, 39]. Considering that the crystalline PCN contained minimum structural defects, the enhanced EPR intensity was concluded to not originate from the structural defects. Instead, this phenomenon was attributed to the novel 3D CFSA structure of U350–670, which exhibited a compact heptazine-based skeleton, minimum structural defects, and a continuous spliced morphology, affording an expanded π -conjugated aromatic system and the enhanced delocalization and mobility of spins [40]. In particular, compared with the slight enhancement in the EPR intensity of U550, U350–670 exhibited a notably enhanced EPR intensity under visible-light irradiation ($\lambda > 470$ nm), further demonstrating the occurrence of the $n \rightarrow \pi^*$ electronic transition in U350–670.

The excitonic processes of U550 and Ux-670 were investigated via steady-state PL measurements. U550 showed one intense emission peak at 462 nm, assigned to the $\pi \rightarrow \pi^*$ electronic transition, indicating the high charge recombination rate of U550 (Fig. 4d) [41]. Alternatively, all the Ux-670 samples showed two emission peaks at 462 and 490 nm, corresponding to the $\pi \rightarrow \pi^*$ and $n \rightarrow \pi^*$ electronic transitions, respectively, consistent with the UV–vis results. The PL intensity of the Ux-670 samples reduced drastically, suggesting the highly suppressed recombination of electron–hole pairs. This result is logical considering that the CFSA structure contained minimum structural defects, which typically serve as electron–hole recombination centers. Moreover, the CFSA

structure with shortened bulk and in-plane diffusion lengths for charge carrier transport enabled the rapid transfer of photoexcited charge carriers in Ux-670, evidenced by its decreased decay lifetime compared with that of U550 in the time-resolved transient PL spectra (Fig. 4e) and the corresponding decay lifetimes (τ , Table S2). Particularly in the case of U350–670, the decay lifetimes (1.27 and 4.61 ns) were considerably smaller than those of U550 (2.59 and 10.06 ns). Next, the separation and migration properties of the photogenerated electron–hole pairs were evaluated using photoelectrochemical spectroscopy. The transient photocurrent of Ux-670 under visible-light irradiation ($\lambda > 420$ nm) was substantially stronger than that of U550 (Fig. 4f), demonstrating the efficient separation of electron–hole pairs in the CFSA structure. Moreover, the CFSA structure achieved considerably improved sluggish charge mobility in pristine PCN. Thus, the electric resistance of Ux-670 is considerably lower than that of U550 based on the distinctly decreased EIS radius of Ux-670 (Fig. 4g), indicating the enhanced charge mobility of Ux-670. Among the Ux-670 samples, U350–670 exhibited the lowest electric resistance and strongest transient photocurrent. In summary, the Ux-670 samples synthesized using the intermediate-induced strategy exhibited superior structural and optical properties than the pristine PCN nanosheets. The U350–670 sample with an advanced 3D CFSA structure and optimal optical properties particularly shows potential as an efficient photocatalyst.

3.4. Hydrogen evolution performance of PCN samples

Finally, the photocatalytic activities of the Ux-670 catalysts were investigated in H_2 evolution reactions in a water/TEOA mixture under visible-light irradiation at ordinary pressure using 1.1 wt% Pt and 10 vol % TEOA as the cocatalyst and electron donor, respectively. The H_2 evolution rates of Ux-670 ($x = 300$ –500) were all above $7400 \mu\text{mol g}^{-1} \text{h}^{-1}$, considerably higher than those of the pristine PCN nanosheets ($1284 \mu\text{mol g}^{-1} \text{h}^{-1}$) and bulk PCN ($71 \mu\text{mol g}^{-1} \text{h}^{-1}$) (Fig. 5a and S11a). In particular, the optimal U350–670 catalyst showed enhanced reusability (Fig. S11b) and a remarkable H_2 generation rate of $14665 \mu\text{mol g}^{-1} \text{h}^{-1}$. In the case of U550–670, which showed a light black color and additional structural damage owing to the excess elimination of nitrogen atoms at high temperatures, a clear enhancement in the photocatalytic activity relative to the pristine PCN nanosheets was observed. These results suggest that the intermediate-induced strategy is an effective method for synthesizing novel PCN-based catalysts with high photocatalytic performance. Fig. 5b illustrates the wavelength-dependent H_2 evolution of U550 and U350–670. The H_2 evolution rate of U350–670 improved notably in the spectral region of 420–600 nm compared with that of U550, consistent with the enhanced utilization of light absorption originating from the $\pi \rightarrow \pi^*$ and $n \rightarrow \pi^*$ electronic transitions [28, 37]. Particularly in the spectral region above 450 nm, U350–670 showed a considerably higher H_2 evolution rate than U550, demonstrating the dominant contribution of the $n \rightarrow \pi^*$ electronic transition to the photocatalytic activity.

4. Conclusions

In summary, using a facile intermediate-induced strategy, we constructed novel PCN nanosheets with a continuous CFSA structure by tuning the condensation degree and repolymerization ability of intermediates. The U350 intermediate with moderate condensation degree and repolymerization ability is the optimal candidate for constructing a superior 3D CFSA structure of PCN. This structure simultaneously exhibits various advantages, such as a 3D framework, small curved nanosheet subunits, high crystallinity, and a partially distorted heptazine-based skeleton, affording abundant reactive sites, shortened bulk and in-plane diffusion lengths for charge carrier transport, improved charge mobility, and enhanced visible-light absorption, respectively. The findings of this study provides a good structural PCN model for realizing the synergistic optimization of the three critical

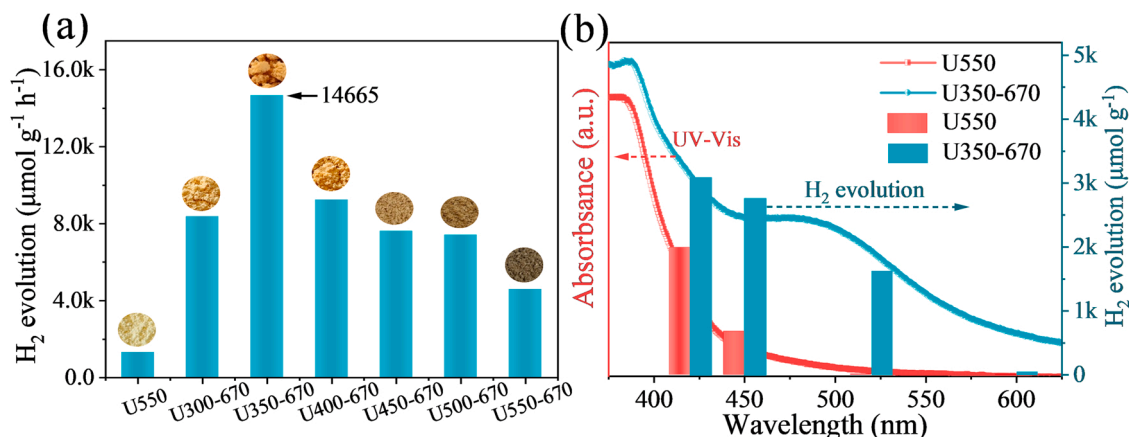


Fig. 5. (a) Photocatalytic H₂ generation of PCN samples under visible-light irradiation (λ > 420 nm, ordinary pressure), (b) the wavelength-dependent H₂ evolution of U550 and U350-670.

processes involved in photocatalysis, i.e., optical absorption, exciton dissociation, and surface reaction.

CRediT authorship contribution statement

S.A. conceived the idea, conducted most of the experiments, analyzed the data, and wrote the manuscript; Y.G., X.H. performed some experiments and analyzed the data; P.G., G.H. conducted some material characterization and analyzed the data; J.H., C.S., X.G. jointly supervised the project, designed the experimental setup, and co-wrote the manuscript. All authors discussed the results, reviewed the manuscript, and approved the final version of the manuscript for submission.

Declaration of Competing Interest

The authors declare that they have no known competing financial interests or personal relationships that could have appeared to influence the work reported in this paper.

Acknowledgements

This work was supported by the National Natural Science Foundation of China (Grant Nos. 21236008), Liao Ning Revitalization Talents Program, China (Program No. XLYC2008032).

Additional information

Additional experimental procedures/data are provided in the [Supplementary Information](#).

Appendix A. Supporting information

Supplementary data associated with this article can be found in the online version at [doi:10.1016/j.apcatb.2022.121323](https://doi.org/10.1016/j.apcatb.2022.121323).

References

- [1] A. Fujishima, K. Honda, Electrochemical photolysis of water at a semiconductor electrode, *Nature* 238 (1972) 37–38.
- [2] Y. Wang, H. Suzuki, J. Xie, O. Tomita, D.J. Martin, M. Higashi, D. Kong, R. Abe, J. Tang, mimicking natural photosynthesis: solar to renewable H₂ fuel synthesis by Z-scheme water splitting systems, *Chem. Rev.* 118 (2018) 5201–5241.
- [3] Q. Wang, K. Domen, particulate photocatalysts for light-driven water splitting: mechanisms, challenges, and design strategies, *Chem. Rev.* 120 (2020) 919–985.
- [4] I.F. Teixeira, E.C.M. Barbosa, S.C.E. Tsang, P.H.C. Camargo, Carbon nitrides and metal nanoparticles: from controlled synthesis to design principles for improved photocatalysis, *Chem. Soc. Rev.* 47 (2018) 7783–7817.
- [5] C. Wang, Y. Hou, J. Cheng, M.-J. Lin, X. Wang, Biomimetic donor-acceptor motifs in carbon nitrides: Enhancing red-light photocatalytic selective oxidation by rational surface engineering, *Appl. Catal. B: Environ.* 294 (2021), 120259.
- [6] X. Wang, K. Maeda, A. Thomas, K. Takanabe, G. Xin, J.M. Carlsson, K. Domen, M. Antonietti, A metal-free polymeric photocatalyst for hydrogen production from water under visible light, *Nat. Mater.* 8 (2009) 76–80.
- [7] G. Gao, Y. Jiao, E.R. Waclawik, A. Du, Single atom (Pd/Pt) supported on graphitic carbon nitride as an efficient photocatalyst for visible-light reduction of carbon dioxide, *J. Am. Chem. Soc.* 138 (2016) 6292–6297.
- [8] J. Liu, H. Wang, M. Antonietti, Graphitic carbon nitride “reloaded”: emerging applications beyond (photo)catalysis, *Chem. Soc. Rev.* 45 (2016) 2308–2326.
- [9] F.K. Kessler, Y. Zheng, D. Schwarz, C. Merschjann, W. Schnick, X. Wang, M. J. Bojdys, Functional carbon nitride materials - design strategies for electrocatalysis, *Nat. Rev. Mater.* 2 (2017) 17030.
- [10] A.J. Rieth, Y. Qin, B.C.M. Martindale, D.G. Nocera, Long-lived triplet excited state in a heterogeneous modified carbon nitride photocatalyst, *J. Am. Chem. Soc.* 143 (2021) 4646–4652.
- [11] J. Qin, J. Barrio, G. Peng, J. Tzadikov, L. Abisdri, M. Volokh, M. Shalom, Direct growth of uniform carbon nitride layers with extended optical absorption towards efficient water-splitting photoanodes, *Nat. Commun.* 11 (2020) 4701.
- [12] Y. Wang, P. Du, H. Pan, L. Fu, Y. Zhang, J. Chen, Y. Du, N. Tang, G. Liu, Increasing solar absorption of atomically thin 2D carbon nitride sheets for enhanced visible-light photocatalysis, *Adv. Mater.* 31 (2019), 1807540.
- [13] W.-J. Ong, L.-L. Tan, Y.H. Ng, S.-T. Yong, S.-P. Chai, Graphitic carbon nitride (g-C₃N₄)-based photocatalysts for artificial photosynthesis and environmental remediation: are we a step closer to achieving sustainability? *Chem. Rev.* 116 (2016) 7159–7329.
- [14] G. Li, Z. Xie, S. Chai, X. Chen, X. Wang, A facile one-step fabrication of holey carbon nitride nanosheets for visible-light-driven hydrogen evolution, *Appl. Catal. B: Environ.* 283 (2021), 119637.
- [15] J. Li, D. Wu, J. Iocozzia, H. Du, X. Liu, Y. Yuan, W. Zhou, Z. Li, Z. Xue, Z. Lin, Achieving efficient incorporation of π-electrons into graphitic carbon nitride for markedly improved hydrogen generation, *Angew. Chem. Int. Ed.* 131 (2019) 2007–2011.
- [16] L. Luo, K. Li, A. Zhang, H. Shi, G. Zhang, J. Ma, W. Zhang, J. Tang, C. Song, X. Guo, Controllable assembly of single/double-thin-shell g-C₃N₄ vesicles via a shape-selective solid-state templating method for efficient photocatalysis, *J. Mater. Chem. A* 7 (2019) 17815–17822.
- [17] J. Zhu, P. Xiao, H. Li, S.A.C. Carabineiro, Graphitic carbon nitride: synthesis, properties, and applications in catalysis, *ACS Appl. Mat. Interfaces* 6 (2014) 16449–16465.
- [18] L. Chen, Y. Wang, S. Cheng, X. Zhao, J. Zhang, Z. Ao, C. Zhao, B. Li, S. Wang, S. Wang, H. Sun, Nitrogen defects/boron dopants engineered tubular carbon nitride for efficient tetracycline hydrochloride photodegradation and hydrogen evolution, *Appl. Catal. B: Environ.* 303 (2022), 120932.
- [19] Z. Fang, Y. Hong, D. Li, B. Luo, B. Mao, W. Shi, One-step nickel foam assisted synthesis of holey g-carbon nitride nanosheets for efficient visible-light photocatalytic H₂ evolution, *ACS Appl. Mater. Interfaces* 10 (2018) 20521–20529.
- [20] P. Niu, L. Zhang, G. Liu, H.-M. Cheng, Graphene-like carbon nitride nanosheets for improved photocatalytic activities, *Adv. Funct. Mater.* 22 (2012) 4763–4770.
- [21] S. Yang, Y. Gong, J. Zhang, L. Zhan, L. Ma, Z. Fang, R. Vajtai, X. Wang, P. M. Ajayan, Exfoliated graphitic carbon nitride nanosheets as efficient catalysts for hydrogen evolution under visible light, *Adv. Mater.* 25 (2013) 2452–2456.
- [22] L. Lin, Z. Yu, X. Wang, Crystalline carbon nitride semiconductors for photocatalytic water splitting, *Angew. Chem. Int. Ed.* 58 (2019) 6164–6175.
- [23] E. Wirmhier, M. Doblinger, D. Gunzelmann, J. Senker, B.V. Lotsch, W. Schnick, Poly[(C₃N₃)₂(NH)_(x)(Li_(1-x))₃LiCl] a crystalline 2D carbon nitride network, *Chemistry* 17 (2011) 3213–3221.

- [24] L. Lin, H. Ou, Y. Zhang, X. Wang, Tri-s-triazine-based crystalline graphitic carbon nitrides for highly efficient hydrogen evolution photocatalysis, *ACS Catal.* 6 (2016) 3921–3931.
- [25] H. Ou, L. Lin, Y. Zheng, P. Yang, Y. Fang, X. Wang, Tri-s-triazine-based crystalline carbon nitride nanosheets for an improved hydrogen evolution, *Adv. Mater.* 29 (2017), 1700008.
- [26] Y. Wang, Y. Guo, Z. Wang, L. Fu, Y. Zhang, Y. Xu, S. Yuan, H. Pan, Y. Du, J. Wang, N. Tang, Realization of strong room-temperature ferromagnetism in atomically thin 2D carbon nitride sheets by thermal annealing, *ACS Nano* 15 (2021) 12069–12076.
- [27] S. An, G. Zhang, K. Li, Z. Huang, X. Wang, Y. Guo, J. Hou, C. Song, X. Guo, Self-supporting 3D carbon nitride with tunable $n \rightarrow \pi^*$ electronic transition for enhanced solar hydrogen production, *Adv. Mater.* (2021), 2104361.
- [28] G. Zhang, G. Li, Z.-A. Lan, L. Lin, A. Savateev, T. Heil, S. Zafeiratos, X. Wang, M. Antonietti, Optimizing optical absorption, exciton dissociation, and charge transfer of a polymeric carbon nitride with ultrahigh solar hydrogen production activity, *Angew. Chem. Int. Ed.* 56 (2017) 13445–13449.
- [29] W. Che, W. Cheng, T. Yao, F. Tang, W. Liu, H. Su, Y. Huang, Q. Liu, J. Liu, F. Hu, Z. Pan, Z. Sun, S. Wei, Fast photoelectron transfer in (Cring)-C₃N₄ plane heterostructural nanosheets for overall water splitting, *J. Am. Chem. Soc.* 139 (2017) 3021–3026.
- [30] J.R. Holst, E.G. Gillan, From triazines to heptazines: deciphering the local structure of amorphous nitrogen-rich carbon nitride materials, *J. Am. Chem. Soc.* 130 (2008) 7373–7379.
- [31] T. Botari, W.P. Huhn, V.W.-H. Lau, B.V. Lotsch, V. Blum, Thermodynamic equilibria in carbon nitride photocatalyst materials and conditions for the existence of graphitic carbon nitride g-C₃N₄, *Chem. Mater.* 29 (2017) 4445–4453.
- [32] G. Zhang, G. Li, T. Heil, S. Zafeiratos, F. Lai, A. Savateev, M. Antonietti, X. Wang, Tailoring the grain boundary chemistry of polymeric carbon nitride for enhanced solar hydrogen production and CO₂ reduction, *Angew. Chem. Int. Ed.* 58 (2019) 3433–3437.
- [33] J. Li, D. Wu, J. Iocozzia, H. Du, X. Liu, Y. Yuan, W. Zhou, Z. Li, Z. Xue, Z. Lin, Achieving efficient incorporation of π -electrons into graphitic carbon nitride for markedly improved hydrogen generation, *Angew. Chem. Int. Ed.* 58 (2019) 1985–1989.
- [34] Z. Chen, A. Savateev, S. Pronkin, V. Papaefthimiou, C. Wolff, M.G. Willinger, E. Willinger, D. Neher, M. Antonietti, D. Dontsova, “The easier the better” preparation of efficient photocatalysts-metastable poly(heptazine imide) salts, *Adv. Mater.* 29 (2017), 1700555.
- [35] S. An, G. Zhang, T. Wang, W. Zhang, K. Li, C. Song, J.T. Miller, S. Miao, J. Wang, X. Guo, High-density ultra-small clusters and single-atom Fe sites embedded in graphitic carbon nitride (g-C₃N₄) for highly efficient catalytic advanced oxidation processes, *ACS Nano* 12 (2018) 9441–9450.
- [36] S. An, G. Zhang, J. Liu, K. Li, G. Wan, Y. Liang, D. Ji, J.T. Miller, C. Song, W. Liu, Z. Liu, X. Guo, A facile sulfur-assisted method to synthesize porous alveolate Fe/g-C₃N₄ catalysts with ultra-small cluster and atomically dispersed Fe sites, *Chin. J. Catal.* 41 (2020) 1198–1207.
- [37] G. Zhang, A. Savateev, Y. Zhao, L. Li, M. Antonietti, Advancing the $n \rightarrow \pi^*$ electron transition of carbon nitride nanotubes for H₂ photosynthesis, *J. Mater. Chem. A* 5 (2017) 12723–12728.
- [38] K.L. Corp, C.W. Schlenker, Ultrafast spectroscopy reveals electron-transfer cascade that improves hydrogen evolution with carbon nitride photocatalysts, *J. Am. Chem. Soc.* 139 (2017) 7904–7912.
- [39] F.-Y. Su, C.-Q. Xu, Y.-X. Yu, W.-D. Zhang, Carbon self-doping induced activation of $n\text{-}\pi^*$ electronic transitions of g-C₃N₄ nanosheets for efficient photocatalytic H₂ evolution, *ChemCatChem* 8 (2016) 3527–3535.
- [40] F. Yang, H. Li, K. Pan, S. Wang, H. Sun, Y. Xie, Y. Xu, J. Wu, W. Zhou, Engineering surface N-vacancy defects of ultrathin mesoporous carbon nitride nanosheets as efficient visible-light-driven photocatalysts, *Sol. RRL* 5 (2020), 2000610.
- [41] L. Luo, Z. Gong, J. Ma, K. Wang, H. Zhu, K. Li, L. Xiong, X. Guo, J. Tang, Ultrathin sulfur-doped holey carbon nitride nanosheets with superior photocatalytic hydrogen production from water, *Appl. Catal. B: Environ.* 284 (2021), 119742.